Editors' Suggestion | Featured in Physics

Perfect Resonant Absorption of Guided Water Waves by Autler-Townes Splitting

L.-P. Euvé,[1] K. Pham,[2] R. Porter,[3] P. Petitjeans,[1] V. Pagneux,[4] and A. Maurel[5]
[1]PMMH, ESPCI Paris, Université PSL, Sorbonne Université, CNRS, 75005 Paris, France
[2]LMI, UME, ENSTA-Paris, Institut Polytechnique de Paris, 91120, Palaiseau, France
[3]School of Mathematics, University Walk, University of Bristol, Bristol BS8 1TW, United Kingdom
[4]LAUM, Avenue Olivier Messiaen, Le Mans Université, CNRS, 72085 Le Mans, France
[5]Institut Langevin, ESPCI Paris, Université PSL, CNRS, 75005 Paris, France

(Received 11 March 2023; accepted 18 September 2023; published 17 November 2023)

The control of guided water wave propagation based on the Autler-Townes splitting resonance concept is demonstrated experimentally, numerically, and theoretically. Complete wave absorption is achieved using an asymmetric pointlike scatterer made of two closely spaced resonant side channels connected to a guide and designed so that its energy leakage is in perfect balance with the inherent viscous losses in the system. We demonstrate that the nature of the resonators and guide junction completely controls the positions of the wave numbers at the reflection and transmission zeros on the real axis; the asymmetry of the resonators completely controls their positions on the imaginary axis. Thus, by adjusting these two independent parameters, we obtain a zero reflection and transmission.

DOI: 10.1103/PhysRevLett.131.204002

Wave phenomena being ubiquitous, the control of waves is an ever-changing field of study, as displayed, for instance, in the last decades by the strong activity in metamaterials [1,2]. Among the many wave controls that can be imagined, absorption is of particular interest since it is able to lead to energy harvesting or noise cancellation. The perfect absorption (PA) of waves by compact devices poses a scientific and technological challenge that has attracted increasing interest in recent years, in optics [3–6], acoustics [7–12], and water waves [13–15]; in the latter context, this is motivated by the need to reduce the reflection of waves in harbors and basins [16,17]. Achieving PA for reflective systems (one-port systems) is relatively easy as a single scattering coefficient, in reflection, is involved. It can be canceled by using a scatterer whose resonance is critically coupled to the system [3,6,8,13]. However, if transmission is allowed (two-port systems), obtaining perfect absorption becomes challenging because it requires the cancellation of both the reflection and transmission coefficients at the same frequency. A neat trick to get around this problem is to use two incident waves, one on each port, with a specific combination of incident amplitudes. A type of perfect absorption, called coherent perfect absorption, is thus obtained by reproducing the sum of two independent critical coupling problems [18,19]. When waves are incident from one side, more sophisticated strategies have been devised using scatterers supporting two resonances. One strategy is to reduce the problem, in a nonsymmetrical way, to a one-port problem with a resonator acting as a mirror over a certain frequency range [20–22]. Another strategy consists of activating, at the same frequency, two symmetric and antisymmetric resonances critically coupled to the system (degenerate resonances) [5,23]. Coupled resonators resulting in electromagnetic induced transparency (EIT) in the lossless case have also been shown to produce enhanced absorption [10].

In this Letter, we propose a new route to perfect absorption that is based on the Autler-Townes splitting (ATS) concept. The ATS, like the EIT, originates from quantum physics. They correspond to limiting cases of strong or weak pumping in a three-level atomic system [24,25], and their classical analogs have been analyzed [26–29]. In [30–32], it has been shown that two identical and closely spaced resonators attached to a guide behave as a point scatterer with monopolar and dipolar resonances leading to rapid variations in transmission and reflection. The appearance of ATS (two transmission zeros at separate, either real or complex conjugate, wave numbers) has been analyzed for an increasing coupling between the resonators fostered by a strong evanescent field; for the classical EIT, in contrast, the interaction is made possible by the interference of waves propagating between two resonators separated by a distance for which the evanescent coupling is negligible.

We consider two closely spaced resonant side channels connected to a waveguide in which water waves propagate (Fig. 1). When the water depth h is constant, a variation $\cosh k(z+h)$ in the depth coordinate z can be factorized from field variables and the resulting problem for the free surface elevation $\eta(x,y)$ becomes analogous to two-dimensional acoustics satisfying

$$\nabla^2\eta + k^2\eta = 0, \tag{1}$$

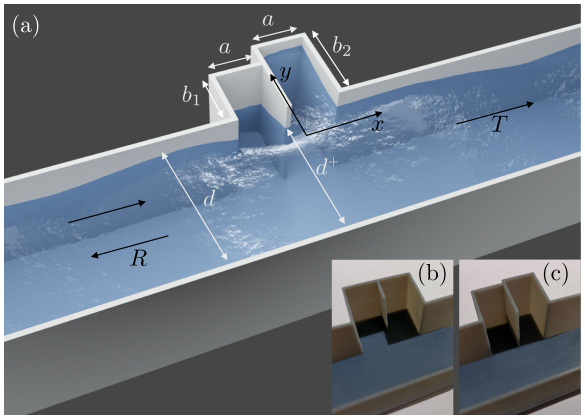

FIG. 1. (a) Conceptual view of the setting made of two closely spaced resonant channels (acting as a scatterer) connected to a guide where water waves propagate; the insets show pictures of the junctions made by 3D printing (b) a symmetric scatterer with $b_1 = b_2$ and (c) an asymmetric scatterer ($b_1 \neq b_2$) used for perfect absorption.

with dispersion $\omega^2 = gk \tanh kh$ (where k is the wave number at frequency ω and g is the gravitational constant). In the following, the PA is going to be achieved by analyzing the wave numbers at the zeros of transmission and reflection in the lossless case, which we want to drive to the same complex value, with the imaginary part exactly compensating the viscous losses induced by friction on the bottom and on the walls. To do this, we rely on the long-wavelength model of [32], which provides explicit expressions for the reflection and transmission coefficients. This allows us to interrogate the qualitative structure of the wave response and reveals the existence and nature of the ATS, thus providing an explicit recipe for tuning the system for PA. In parallel, we perform direct numerical calculations of the solution (i.e., without making any assumptions about long wavelengths, see Appendix A for details) and compare the results with experiments.

Analysis and experimental evidence of ATS.—To demonstrate the ATS mechanism, that is to say, the strong evanescent coupling between the two resonators leading to two distinct zeros of transmission, we begin with the problem of a symmetric scatterer (two identical resonant side channels with heights $b = b_1 = b_2$ in Fig. 1), whose features will provide an important guide for the discussion of asymmetric scatterers (detuned side channels with $b_1 \neq b_2$). Note that evanescent coupling can be tuned by varying the ratio d^+/d, see Appendix B. The analysis that follows is made on the assumption of long waves equivalent to a low frequency approximation. Thus, in the guide, only the plane mode propagates and far enough away from the scattering region at $x = 0$, $\eta(x, y) \simeq \eta(x)$. For an incoming wave from the left with wave number k and complex amplitude A^{inc}, the free surface elevation is $\eta(x) = A^{\text{inc}}(e^{ikx} + R_0 e^{-ikx})$, $x < 0$, and $\eta(x) = A^{\text{inc}} T_0 e^{ikx}$, $x > 0$, with the time dependence convention $e^{-i\omega t}$ and with (R_0, T_0) as the complex-valued reflection and transmission coefficients. Following [32], the effect of the scatterer is replaced by jump conditions, at $x = 0$, on η and its derivative with respect to x; these jumps involve four real dimensionless parameters $(\delta_a, \delta_s, \delta_0, \delta)$ that depend only on the geometry of the junction d/a [32], with d as the guide width and a as the channel width, see Fig. 1; see also Sec. I of the Supplemental Material [33].

Close to the resonance frequency that occurs at $kb \sim \pi/2$, (R_0, T_0) can then be written as

$$R_0 = -i\frac{a}{db}\frac{(k-\kappa_0)}{(k-k_0^+)(k-k_0^-)}, \quad T_0 = \frac{(k-\kappa_0^+)(k-\kappa_0^-)}{(k-k_0^+)(k-k_0^-)}, \tag{2}$$

where $\kappa_0, \kappa_0^\pm$ are the zeros of R_0 and T_0 and $k_0^\pm$ are the poles of the scattering matrix, which take the form

$$\kappa_0 = \frac{\pi}{2b} - \frac{a}{b^2}\delta_a, \quad \kappa_0^\pm = \frac{\pi}{2b} - \frac{a}{b^2}(\delta_0 \mp \sqrt{\Delta_0}),$$
$$k_0^- = \frac{\pi}{2b} - \frac{a}{b^2}\delta_s - \frac{ia}{db}, \quad k_0^+ = \frac{\pi}{2b} - \frac{a}{b^2}\delta_a - \frac{iad}{b^3}\delta^2, \tag{3}$$

with $\Delta_0 = (\delta_0 - \delta_a)^2 - \delta^2$. It can be remarked that the wave number κ_0 corresponding to zero reflection is always real, resulting in a transparent window in the transmission spectrum. In contrast, the wave numbers $\kappa_0^\pm$ at the two transmission zeros experience a transition [34] from complex conjugates ($\Delta_0 < 0$) to purely real ($\Delta_0 > 0$) when increasing d/a. This is confirmed in Fig. 2 where we report results from direct numerics in the two-dimensional setting varying d/a and b/a at given a. We show the critical curve $(d/a)_c$ above which the wave numbers at the zeros of T_0 are real. The insets (a)–(c) show typical profiles of $|R_0|$ and $|T_0|$ against wave number k, revealing the characteristic

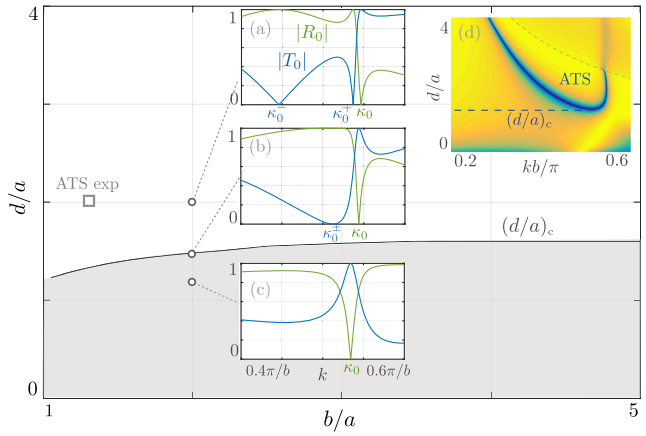

FIG. 2. Critical curve $(d/a)_c$ against b/a from direct numerics. (a)–(c) typical variations of (R_0, T_0) vs wave number k with two perfect transmission zeros at real wave numbers $\kappa_0^\pm$ for $d/a > (d/a)_c$ and weak transmission dips for $d/a < (d/a)_c$. (d) Transmission spectrum for $b/a = 4/3$ as used in the ATS experiment.

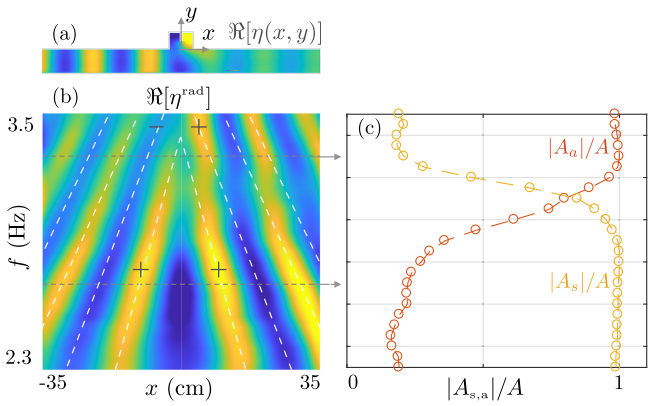

FIG. 3. Experimental ATS; monopolar and dipolar resonances. (a) $\mathrm{Re}[\eta(x,y)]$, the real part of $\eta(x,y)$, measured at $f = 3.3$ Hz. (b) Real part of the radiated field $\mathrm{Re}[\eta^{\mathrm{rad}}(x)]$ vs f, revealing a transition from monopolar to dipolar resonances. (c) Normalized symmetric A_s and antisymmetric A_a channel amplitudes vs f ($A = |A_1| + |A_2|$).

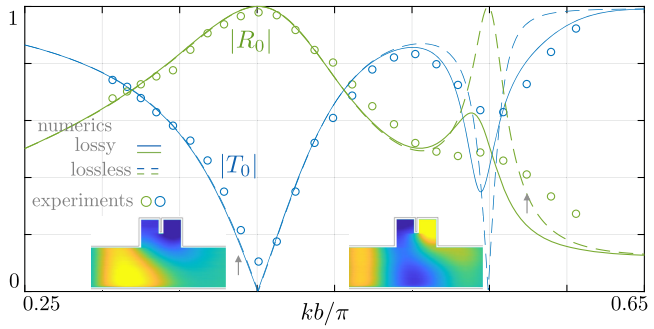

FIG. 4. Scattering coefficients vs nondimensional wave number, experiments (symbols), and numerics (lossy case, plain line; lossless case, dashed lines). The insets show $\mathrm{Re}[\eta(x,y)]$ at $f = 2.7$ and $f = 3.3$ Hz (arrows).

splitting of the two transmission zeros at real wave numbers $\kappa_0^{\pm}$ as d/a is increased beyond $(d/a)_c$. Note that the model predicts that the critical curve $(d/a)_c$ ($\Delta_0 = 0$) is independent of the channel length b; numerically, we observe a dependence (albeit quite weak) with b that is not accounted for in the model [the model provides the asymptote $(d/a)_c = 1.8$ for large b/a].

In the experiment, we use $d = 6$, $b = 4$, and $a = 3$ cm with a 140 cm long guide and a water depth $h = 5$ cm. Waves at frequencies $f \in (2.3, 3.7)$ Hz are generated using a plunging-type wave maker guided by a linear motor and placed at the left end of the guide (typical wavelength is 20 cm). We benefit from space-time resolved measurements from which, for each frequency, the complex field $\eta(x,y)$ can be deduced by Fourier transform of real time signals [35–37]; see Appendix C for details. An example of such a field is shown in Fig. 3(a) for $f = 3.3$ Hz ($kb = 0.55\pi$). At this frequency, only the plane mode is propagating and, in the experiment, we observe that $\eta(x,y) \simeq \eta(x)$ in reflection and transmission except in the vicinity of $x = 0$. Here, the field is two-dimensional due to the presence of the evanescent field triggered by the junction. Therefore, we identify the complex incident amplitude A^{inc} and the scattering coefficients (R_0, T_0) by taking measurements far enough from this region [and, in practice, $\eta(x)$ is obtained by averaging $\eta(x,y)$ over y]. We also measure the complex amplitudes A_1 and A_2 on the end walls of the channels. Figure 3(b) shows the field radiated, or emitted, by the scatterer $\eta^{\mathrm{rad}}(x) = [\eta(x) - \eta^{\mathrm{inc}}(x)]/A^{\mathrm{inc}}$ where $\eta^{\mathrm{inc}}(x) = A^{\mathrm{inc}} e^{ikx}$. We observe a symmetrical, monopolar emission up to $f \simeq 3.1$ Hz, then a progressive phase shift of the transmitted wave leads to an asymmetrical, dipolar emission. This is confirmed by the symmetric and antisymmetric amplitudes in the side channels, $A_s = (A_1 + A_2)$ and $A_a = (A_1 - A_2)$, whose variations as a function of f, normalized to $A = |A_1| + |A_2|$, are reported in Fig. 3(c). We observe that $|A_s|/A \simeq 1$ when the monopolar resonance is dominant ($A_1 \simeq A_2$ are in phase) and that $|A_a|/A \simeq 1$ when the dipolar resonance is dominant ($A_1 \simeq -A_2$ are out of phase).

The scattering coefficients $(|R_0|, |T_0|)$ as a function of frequency are shown in Fig. 4, highlighting the ATS with two dips in transmission (zero transmission in the lossless case). The monopolar resonance ($kb = 0.40\pi$) is very weakly affected by the losses, which leads to an almost zero transmission in good agreement with the direct numerics (dashed lines in the lossless case); on the other hand, the dipole resonance is significantly weakened with a transmission dip at $kb \simeq 0.55\pi$ which does not go to zero. In the model, the frequencies at monopole resonance ($\kappa_0^- b = 0.44\pi$) and at dipole resonance ($\kappa_0^+ b = 0.56\pi$) are consistent with our measurements and each is associated with a near pole $k_0^{\pm}$ [with $k_0^- b = (0.46 - 0.16i)\pi$ and $k_0^+ b = (0.57 - 0.01i)\pi$]. Furthermore, the leakage of the two resonances given by the imaginary parts of $k_0^{\pm}$ differ by a factor of 16, which is what we see in the experiment (when measuring for the two resonances, the ratio of the half-value widths or the absorption $\alpha = 1 - |R_0|^2 - |T_0|^2$) and what we used for the direct numerics in the lossy case shown by plain lines in Fig. 4. In doing so, however, we note mismatches between experiments and direct numerical calculations, which are partly attributable to imperfect modeling of the frequency dependence of losses in the experiments and partly to unaccounted-for effects such as the nonlinearities inherent in the experiments.

Analysis and experimental realization of PA.—The PA is obtained by analyzing the wave numbers associated with zero transmission and zero reflection in the lossless case, which we want to bring to the same complex value; this complex value will be compensated by the losses afterward in the experiments [38]. According to what we have seen previously, this is not possible using a symmetrical scatterer because the wave number at zero reflection is always real. We will see that this is no longer the case for a

nonsymmetric scatterer; we now consider an asymmetry parameter ε defined by $b_1 = b(1-\varepsilon)$, $b_2 = b(1+\varepsilon)$, with $|\varepsilon| < 1$ (Fig. 1). Extending the model of [32] for different channel heights, we obtain near the resonance at $kb \simeq \pi/2$ the new form of the scattering coefficients,

$$R = -i\frac{a}{db}\frac{(k-\kappa)}{(k-k^+)(k-k^-)}, \quad T = \frac{(k-\kappa^+)(k-\kappa^-)}{(k-k^+)(k-k^-)}, \tag{4}$$

with

$$\kappa = \kappa_0 + i\frac{\pi d}{b^2}\delta\varepsilon, \quad \kappa^\pm = \frac{\pi}{2b} - \frac{a}{b^2}(\delta_0 \mp \sqrt{\Delta}), \tag{5}$$

and $\Delta = \Delta_0 + (\pi b/2a)^2\varepsilon^2$ (see Sec. I of the Supplemental Material [33]). Compared to (3), we notice that the asymmetry shifts the wave numbers at zero transmission; as we will consider a reference case with $\Delta_0 < 0$, it only affects the imaginary part of $\kappa^\pm$. In parallel, the wave number at zero reflection acquires a complex value proportional to ε. We are now able to move to the PA without the need for a complex optimization process by performing $\kappa = \kappa^+$ (the zero of transmission with positive imaginary value) with two very simple steps: in step 1 we will first ensure equal real parts and, subsequently, in step 2 we will achieve equal imaginary parts.

Step 1: $\mathrm{Re}(\kappa) = \mathrm{Re}(\kappa^+)$—if $\Delta < 0$ (which implies $\Delta_0 < 0$); this condition is the same as $\mathrm{Re}(\kappa_0) = \mathrm{Re}(\kappa_0^+)$ since the wave numbers have a real part independent of ε. According to (3) and (5) this condition is realized when

$$\delta_0 = \delta_a. \tag{6}$$

Step 2: $\mathrm{Im}(\kappa) = \mathrm{Im}(\kappa^+)$. This equality requires

$$\left[1 + \left(\frac{2\delta d}{b}\right)^2\right]\varepsilon^2 = \left(\frac{2\delta}{\pi}\frac{a}{b}\right)^2. \tag{7}$$

If we add the condition (6) on d/a, the above condition provides a one-to-one correspondence between (b/d) and $\varepsilon = \varepsilon_{\mathrm{PA}}$ realizing $\kappa = \kappa^+$, which is necessary to achieve perfect absorption when losses are taken into account.

To design our experimental setup, we followed the above procedure to obtain an initial guess and then used an iterative test on experimental measurements, which allows us to eventually find the values $a = 2.63$, $b_1 = 3.24$, and $b_2 = 3.64$ cm ($\varepsilon = 0.058$), which fall very close to our prediction (see Appendix B). The PA is demonstrated and analyzed in Figs. 5 and 6. We first plot the field $\eta(x,y)$ measured at $f = 2.9$ Hz and the corresponding profile $\eta(x)$ averaged along y in the guide and normalized to the incident amplitude, see Fig. 5(a), where negligible transmission and reflection are realized. This is confirmed in Fig. 6(a) where we plot the variations of the (R,T) measured experimentally vs kb/π; these variations are well reproduced by direct numerics using constant losses $k_i = 0.023$ cm^{-1}.

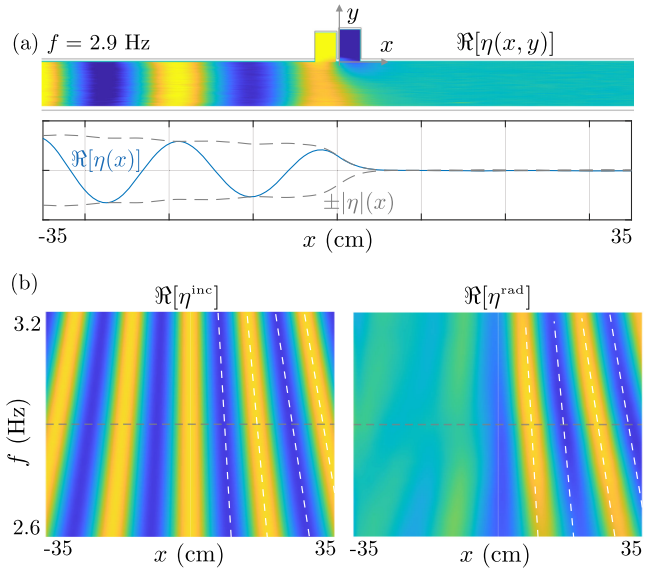

FIG. 5. Experimental measurements of the wave field for the perfect absorption. (a) 2D field of the surface elevation $\eta(x,y)$ and mean profile $\eta(x)$ (real part and amplitude) at $f = 2.9$ Hz with no reflection [no beating of $|\eta|(x)$ for $x < 0$] and no transmission [$\eta(x) = 0$ for $x > 0$]. (b) Profiles of the incident $\eta^{\mathrm{inc}}(x)$ and radiated $\eta^{\mathrm{rad}}(x)$ waves vs frequency.

Perfect absorption is obtained because the scatterer is able to radiate strongly anisotropically (toward $x < 0$ and $x > 0$) in phase, which was already the case in the symmetric case but here also in amplitude. In Fig. 5(b), we have plotted $\eta^{\mathrm{inc}}(x)$ and $\eta^{\mathrm{rad}}(x)$ as functions of f, as in Fig. 3(a). The anisotropy is clearly visible and the conditions $\eta^{\mathrm{rad}}(x < 0) \simeq 0$ and $\eta^{\mathrm{rad}}(x > 0) \simeq -\eta^{\mathrm{inc}}(x > 0)$ are satisfied. This nonsymmetric emission is made possible by a balance between the amplitudes A_1 and A_2 in the side channels, resulting in a balance between the symmetric A_s and antisymmetric A_a amplitudes shown in Fig. 6(b). We observe that these contributions are 90° out of phase with a

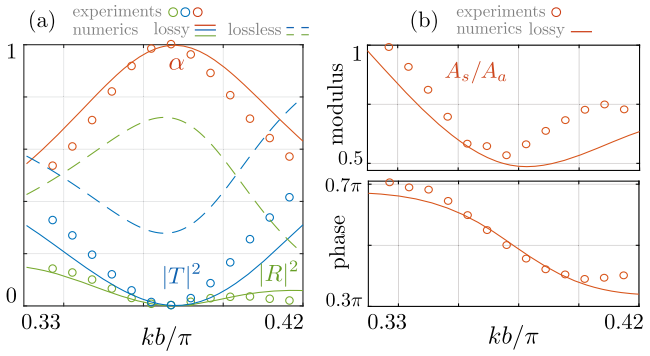

FIG. 6. Experimental PA. (a) Reflection $|R|^2$, transmission $|T|^2$, and absorption α against nondimensional frequency kb/π. (b) modulus and phase of A_s/A_a.

ratio $A_s/A_a \sim 0.5$ at the PA. Interestingly, this relationship is consistent with a calculation in which the two channels are replaced by two point sources separated by a distance $a/2$ and imposing amplitudes (A_1, A_2) with $A_1 = -A_2 e^{ika}$ (see Sec. II of the Supplemental Material [33]).

In conclusion, we have demonstrated, experimentally and theoretically, the Autler-Townes splitting for a symmetric scatterer interacting with waves propagating in a guide. By extending the model to the case of nonsymmetric scatterers, we have obtained a simple procedure to achieve perfect absorption by shifting, in the complex plane, the wave numbers producing the transmission and reflection zeros to exactly the same value, chosen in such a way as to compensate exactly the inherent losses in the system. The approach we are following and the resulting phenomenology are not restricted to water waves, and thus, our findings could find applications to all domains of wave physics, from matter to electromagnetic and optical waves. We foresee that the proposed strategy, using asymmetric configuration of evanescently coupled resonators, opens new directions to achieve perfect subwavelength absorption; in particular, it would be interesting to extend our analysis to the case of a scatterer formed by $N > 2$ resonators with N governing the number of resonances.

The authors acknowledge the support of the ANR under Grants No. 243560 CoProMM and No. ANR-19-CE08-0006, and of the Agence de l'Innovation de Défense from DGA under Grant No. 2019 65 0070.

Appendix A: Numerical method.—Direct numerical calculations were performed by solving (1) using a multimodal method as in [32]. This consists of writing the two-dimensional field in each domain of constant width $d(j) = (d, (d + b_1), d^+, (d + b_2), d), \quad j = 1, \ldots, 5$ in the form

$$\eta^{(j)}(x, y) = \sum_{n=0}^{\infty} (a_n(j) e^{ik_n(j)x} + b_n(j) e^{-ik(j)_n x}) E(j)_n(y), \tag{A1}$$

with the $E_n(j)(y) = \cos(n\pi y/d(j))$ forming a basis of transverse functions satisfying the boundary conditions at $y = 0$ and $d(j)$ and $k_n^{(j)} = \sqrt{k^2 - (n\pi/d^{(j)})^2}$ forming the wave numbers along x. The problem is then solved classically by projecting the continuity conditions of η and $\partial_x \eta$ onto the transverse functions at each width discontinuity. The resulting system, after truncation of the series in (A1), is then inverted to obtain the reflection coefficients $R_n = b_n^{(1)}$ (the incident wave being associated with $a_n^{(1)} = 1$), the transmission coefficients $T_n = a_n^{(5)}$ (with $b_n^{(5)} = 0$, which takes into account the radiation condition), and the amplitudes $(a_n^{(j)}, b_n^{(j)})$, $j = 2, 3, 4$, hence the whole complex field $\eta(x, y)$. In the lossy case, we simply consider $k = k_r + ik_i$. For Fig. 4, we used $k_i b = 0.01\pi \exp\{-[(kb - 0.57\pi)/0.03b]^2\}$, which produces the expected losses $k_i \simeq 10^{-3}$ cm^{-1} in the vicinity of the resonance at $k_r = 0.57\pi/b$. For Fig. 6, we simply used constant k_i given by the imaginary part of κ.

Appendix B: Additional information on the ATS and PA experiments.—The ATS experiment aims to demonstrate, for $b_1 = b_2$, the realization of two distinct transmission dips at two real wave numbers (in the lossless case, two perfect transmission zeros). To do this, we used a junction region that fosters evanescent coupling between the side channels; specifically, communication between them was made easier by shifting the position of the partition wall, $d^+ > d$ as shown in the inset of Fig. 1(a) (we used $d = 6$, $d^+ = 8$ cm for $a = 3$ cm). The resulting effective parameters $(\delta_a, \delta_s, \delta_0, \delta)$, which are independent of b and frequency, are for this "junction 1": $\delta_a = -0.2831$, $\delta_s = 0.1501$, $\delta_0 = -0.0069$, $\delta = 0.1420$, resulting in $\Delta = \Delta_0 = 0.056 > 0$, according to the numerical results of Fig. 1, slightly above the critical value $(d/a)_c \sim 1.6$ realizing $\Delta_0 = 0$ (in the model, this value is independent of b/a, while the numerics show a variation for small b/a values).

In the PA experiments, we want complex wave numbers at the transmission zeros, which, from (5), requires $\Delta_0 < 0$. As this condition implies small (d/a), which would increase losses due to viscous effects in the waveguide, we move to a junction (named junction 2) for which the partition wall is flush with the guide wall ($d^+ = d$). The numerically determined resulting critical curve $(d/a)_c$ is

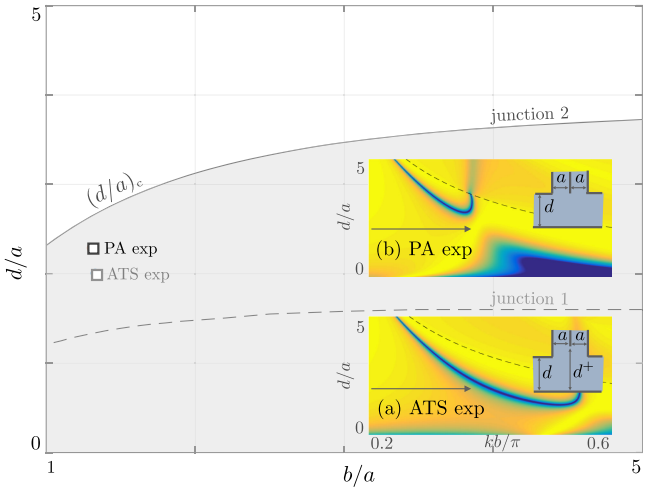

FIG. 7. Critical curves $(d/a)_c$ for junction 1 (ATS exp) and for junction 2 (PA exp) obtained from direct numerics. (a) The transmission spectrum for $b/a = 4/3$ as used in the ATS experiment. (b) The transmission spectrum for $b/a = 1.31$ as used in the PA experiment. (a),(b) We report the geometry of the junctions; $d/a = 3$ and $d^+/a = 4$ for junction 1, $d/a = 2$ for junction 2. The arrows show the values of d/a in the experiments.

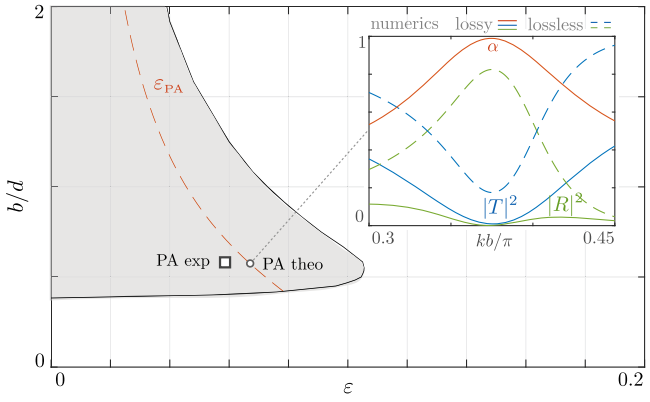

FIG. 8. PA for $\varepsilon = \varepsilon_{\mathrm{PA}}$ against b/d [dashed red line from (5)]. Outside the shaded region, ATS takes place, resulting in real-valued $\kappa^{\pm}$. For $b/d = 0.57$, PA is achieved theoretically at circle (PA theo) and experimentally at square (PA exp). The inset shows the numerical PA with $\alpha \simeq 1$.

significantly shifted toward higher d/a values compared to that of junction 1, as shown in Fig. 7 [and, as for junction 1, we observe a dependence of $(d/a)_c$ on b/a, whereas the model only provides the asymptotic value $(d/a)_c = 3.7$ for large b/a, see Ref. [32]].

To design our experimental setup, we start by following the two-step procedure [(6) and (7)] corresponding to the theoretical conditions of the PA. In the first step, (6) requires that $\delta_0 = \delta_a$ (which depends only on d/a, the junction geometry). We find that this condition is met for $d/a = 3.0$, which fixes the values of the four parameters; namely, we have for this "junction 2" $\delta_a = \delta_0 = 0.6812$, $\delta_s = 0.6498$, and $\delta = 0.2476$.

With $(d/a) = 3.0$ from the previous step, (7) provides a simple condition between b/d and ε only. The resulting curve $\varepsilon = \varepsilon_{\mathrm{PA}}$ against b/d is shown in Fig. 8 (red dotted line). For completeness, we also show the shaded region (obtained numerically) within which the ATS with two distinct complex transmission zeros is observed. By construction, each pair $(b/d, \varepsilon)$ realizes $\kappa^+ = \kappa$, and we want now their imaginary part (in the lossless case) to be exactly compensated by the viscous losses. In our experiments, we expect the losses to be well described by a wave number whose imaginary part is $k_i \in (0.02, 0.03)$ cm^{-1}. From (5), this reduces the allowable ranges along the $\varepsilon = \varepsilon_{\mathrm{PA}}$ curve to $b/d \in (0.55, 0.65)$ and $\varepsilon \in (6.3, 6.9) \times 10^{-2}$. The inset in Fig. 8 shows the PA obtained numerically for a particular point of this curve for $k_i = 0.026$ cm^{-1} (the lossless case is shown for comparison) with an absorption reaching $\alpha = 1 - |R|^2 - |T|^2 \simeq 1$. As mentioned earlier, this analysis was used as a starting point in the experiments. The PA observed in Fig. 8 provides, if we use a waveguide with $d = 6$ cm, the values of $a = 2.0$, $b_1 = 3.21$, and $b_2 = 3.67$ cm. We found that $a = 2.63$, $b_1 = 3.24$, and $b_2 = 3.64$ cm produce higher absorption, as demonstrated in the main text (the square in Fig. 8 which is close to the theoretical curve).

Appendix C: Experimental FTP measurement.—This measurement technique is based on the analysis of local displacements of fringes projected onto the free surface at rest and disturbed by wave propagation, which allows a measurement of the real-valued free surface elevation $\eta_t(x, y, t)$ recorded by a high speed camera. The complex-valued free surface elevation $\eta(x, y)$ is then obtained by Fourier transform $\eta(x, y) = \int_0^{t_f} \eta_t(x, y, t) e^{i\omega t} dt$, with ω the working frequency imposed by the wave generator and t_f corresponding to several $2\pi/\omega$ periods [35–37]. We use a camera with 1936×1216 pixels, which gives a spatial resolution $\delta x = \delta y = 0.4$ mm/pixel on a 75 cm wide region of the guide (including the height of the guide and channels) and a temporal resolution given by the camera acquisition speed $\delta t = 50$ ms.

[1] N. Engheta and R. W. Ziolkowski, *Metamaterials: Physics and Engineering Explorations* (John Wiley & Sons, New York, 2006).
[2] R. V. Craster and S. Guenneau, *Acoustic Metamaterials: Negative Refraction, Imaging, Lensing and Cloaking* (Springer Science & Business Media, New York, 2012), Vol. 166.
[3] A. Yariv, IEEE Photonics Technol. Lett. **14**, 483 (2002).
[4] T. S. Luk, S. Campione, I. Kim, S. Feng, Y. C. Jun, S. Liu, J. B. Wright, I. Brener, P. B. Catrysse, S. Fan *et al.*, Phys. Rev. B **90**, 085411 (2014).
[5] J. R. Piper, V. Liu, and S. Fan, Appl. Phys. Lett. **104**, 251110 (2014).
[6] J. R. Piper and S. Fan, ACS Photonics **1**, 347 (2014).
[7] X. Cai, Q. Guo, G. Hu, and J. Yang, Appl. Phys. Lett. **105**, 121901 (2014).
[8] P. Wei, C. Croënne, S. Tak Chu, and J. Li, Appl. Phys. Lett. **104**, 121902 (2014).
[9] M. Yang, C. Meng, C. Fu, Y. Li, Z. Yang, and P. Sheng, Appl. Phys. Lett. **107**, 104104 (2015).
[10] A. Merkel, G. Theocharis, O. Richoux, V. Romero-García, and V. Pagneux, Appl. Phys. Lett. **107**, 244102 (2015).
[11] V. Romero-García, G. Theocharis, O. Richoux, A. Merkel, V. Tournat, and V. Pagneux, Sci. Rep. **6**, 19519 (2016).
[12] A. Maurel, J.-F. Mercier, K. Pham, J.-J. Marigo, and A. Ourir, J. Acoust. Soc. Am. **145**, 2552 (2019).
[13] E. Monsalve, A. Maurel, P. Petitjeans, and V. Pagneux, Appl. Phys. Lett. **114**, 013901 (2019).
[14] R. Porter, Appl. Ocean Res. **113**, 102724 (2021).
[15] B. Wilks, F. Montiel, and S. Wakes, J. Fluid Mech. **941**, A26 (2022).
[16] H. Martins-Rivas and C. C. Mei, J. Fluid Mech. **626**, 395 (2009).
[17] I. Theocharis, E. N. Anastasaki, C. I. Moutzouris, and T. Giantsi, Ocean Eng. **38**, 1967 (2011).
[18] Y. D. Chong, L. Ge, H. Cao, and A. D. Stone, Phys. Rev. Lett. **105**, 053901 (2010).
[19] W. Wan, Y. Chong, L. Ge, H. Noh, A. D. Stone, and H. Cao, Science **331**, 889 (2011).

[20] N. Jiménez, V. Romero-García, V. Pagneux, and J.-P. Groby, Sci. Rep. **7**, 13595 (2017).
[21] W. R. Sweeney, C. W. Hsu, S. Rotter, and A. D. Stone, Phys. Rev. Lett. **122**, 093901 (2019).
[22] S. Soleymani, Q. Zhong, M. Mokim, S. Rotter, R. El-Ganainy, and Ş. Özdemir, Nat. Commun. **13**, 599 (2022).
[23] V. Romero-García, N. Jiménez, J.-P. Groby, A. Merkel, V. Tournat, G. Theocharis, O. Richoux, and V. Pagneux, Phys. Rev. Appl. **14**, 054055 (2020).
[24] S. H. Autler and C. H. Townes, Phys. Rev. **100**, 703 (1955).
[25] N. B. Delone and V. P. Krainov, Phys. Usp. **42**, 669 (1999).
[26] C. Garrido Alzar, M. Martinez, and P. Nussenzveig, Am. J. Phys. **70**, 37 (2002).
[27] A. A. Abdumalikov Jr, O. Astafiev, A. M. Zagoskin, Y. A. Pashkin, Y. Nakamura, and J. S. Tsai, Phys. Rev. Lett. **104**, 193601 (2010).
[28] P. M. Anisimov, J. P. Dowling, and B. C. Sanders, Phys. Rev. Lett. **107**, 163604 (2011).
[29] G. Andersson, M. K. Ekström, and P. Delsing, Phys. Rev. Lett. **124**, 240402 (2020).
[30] Y. Jin, Y. Pennec, and B. Djafari-Rouhani, J. Phys. D **51**, 494004 (2018).
[31] Y. Liu, A. Talbi, El Houssaine El Boudouti, O. Bou Matar, P. Pernod, B. Djafari-Rouhani, and B. Djafari-Rouhani, Phys. Rev. Appl. **11**, 064066 (2019).
[32] R. Porter, K. Pham, and A. Maurel, Phys. Rev. B **105**, 134301 (2022).
[33] See Supplemental Material at http://link.aps.org/supplemental/10.1103/PhysRevLett.131.204002 for the SM presents details on the theoretical model and on the relation between the symmetric and antisymmetric amplitudes channel amplitudes.
[34] Y. Kang, A. Z. Genack, Phys. Rev. B **103**, L100201 (2021).
[35] A. Maurel, P. Cobelli, V. Pagneux, and P. Petitjeans, Appl. Opt. **48**, 380 (2009).
[36] P. J. Cobelli, A. Maurel, V. Pagneux, and P. Petitjeans, Exp. Fluids **46**, 1037 (2009).
[37] A. Przadka, B. Cabane, V. Pagneux, A. Maurel, and P. Petitjeans, Exp. Fluids **52**, 519 (2012).
[38] V. Romero-García, G. Theocharis, O. Richoux, and V. Pagneux, J. Acoust. Soc. Am. **139**, 3395 (2016).